

Inverse design of potential metastructures inspired from Indian medieval architectural elements

Bishakh Bhattacharya¹, Tanuj Gupta¹, Arun Kumar Sharma¹,
Ankur Dwivedi¹, Vivek Gupta², Subhadeep Sahana¹,
Suryansh Pathak³, and Ashish Awasthi¹

¹Indian Institute of Technology Kanpur, India
{bishakh@iitk.ac.in, tanujg21@iitk.ac.in}

²Delft University of Technology, Netherlands

³Motilal Nehru National Institute of Technology Allahabad, India

Abstract

In this study, we immerse in the intricate world of patterns, examining the structural details of Indian medieval architecture for the discovery of motifs with great application potential from the mechanical metastructure perspective. The motifs that specifically engrossed us are derived from the tomb of I'timad-ud-Daula, situated in the city of Agra, close to the Taj Mahal. In an exploratory study, we designed nine interlaced metastructures inspired from the tomb's motifs. We fabricated the metastructures using additive manufacturing and studied their vibration characteristics experimentally and numerically. We also investigated bandgap modulation with metallic inserts in honeycomb interlaced metastructures. The comprehensive study of these metastructure panels reveals their high performance in controlling elastic wave propagation and generating suitable frequency bandgaps, hence having potential applications as waveguides for noise and vibration control. Finally, we developed novel AI-based model trained on numerical datasets for inverse design of metastructures with a desired bandgap.

Keywords: Metamaterials, Metastructures, Interlaced metastructures, Hierarchical Metastructures, Fractals, Honeycomb, Elastic wave control, Artificial Intelligence, Multihead geometric attention, Multiscale residual network, Inverse design.

Introduction

Architectural intricate patterns have a long history, with certain examples dating back to the 4th century [1]. However, these early forms were the outcome of creative heuristic advancements of pattern generation in human civilization. It wasn't until the late 19th century, when fundamental physics became better understood, that the development of systematic engineering principles made it possible to explore counter-intuitive physical characteristics of some patterns in periodic structures, generally known as metamaterials and metastructures. Today, it is often proposed as a panacea for controlling attenuation and wavefront divergence related to elastic and electromagnetic wave propagation and there exists a vast literature of which are based on meticulously designed lattice structures with special geometric patterns [2–6]. These engineered lattices may introduce exotic mechanical and electromagnetic properties, manipulating the behavior of electromagnetic waves [7], elastic waves as well as sound waves [8–11]. By carefully designing these lattices, scientists can achieve extraordinary effects like negative stiffness [12], negative mass [13], and negative Poisson's ratio [14]. The study of lattice geometries in metamaterials opens a pathway to myriad innovative applications ranging from optics to acoustics, wearable devices [15, 16], advanced space structures [17, 18], next-gen automobiles [19, 20], robotic manipulators [21], bionic grippers, [22] and anti-seismic structures [23, 24]. These metamaterials exhibit characteristics such as high specific stiffness [25–28], negative Poisson's ratio [29, 30], negative thermal expansion coefficient [31], negative reflection [32, 33], wave alteration [34], sub-wavelength bandgap [35, 36] and distinctive electrodynamic phenomena [37, 38]. The generation of a large range of novel periodic structures at different length scales has ushered in phenomenal developments of metamaterials.

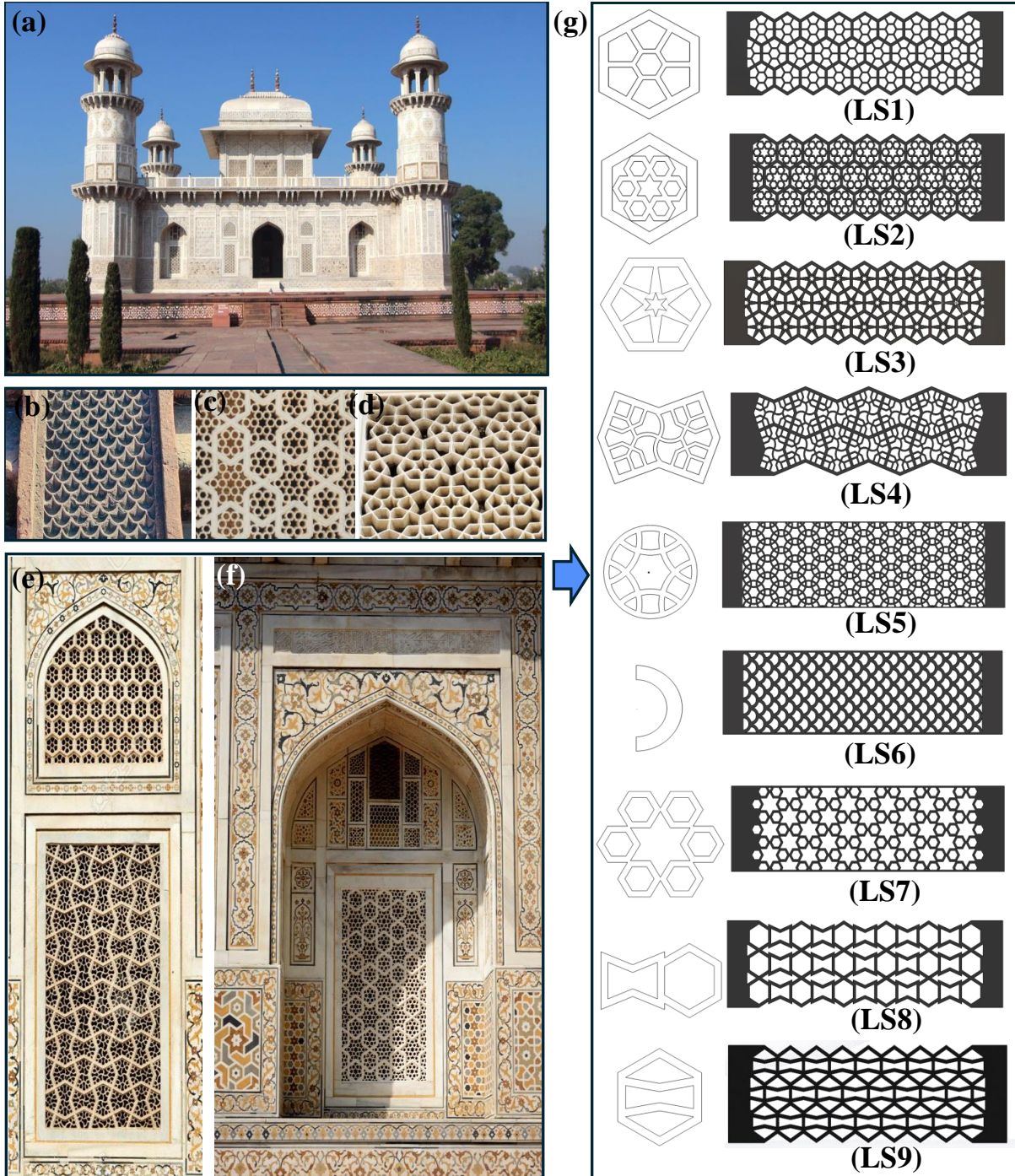


Figure 1: The Tomb of Itmad-ud-Daula is a Mughal mausoleum in the city of Agra in the Indian state of Uttar Pradesh (27.1929 ° N, 78.0310 ° E). The architecture of this monument is unique in terms of crafting which uses a combination of pietra-dura and calligraphy-based decorative art techniques. It is considered to be the pioneer of the creation of funerary tombs in Mughal-India which was subsequently magnified in the Taj Mahal. However, with its marble latticework and exquisite carvings, the tomb is considered as a work of art even more delicate than the Taj Mahal. **(b to d)**. Consequently, the latticework is depicted through the carved panels of calligraphic design. The walls, floors, and niches are decorated with beautiful geometrical patterns. **(e and f)**. Here, we have specifically focused on the Jali screens at the centre of the niches all around the tomb. They were used extensively during the Mughal reign for elegance and their ability to facilitate the entry of natural light and air inflow. Often it is also used as part of a passive cooling system. **(g)** shows the corresponding structural models (LS1-LS9).

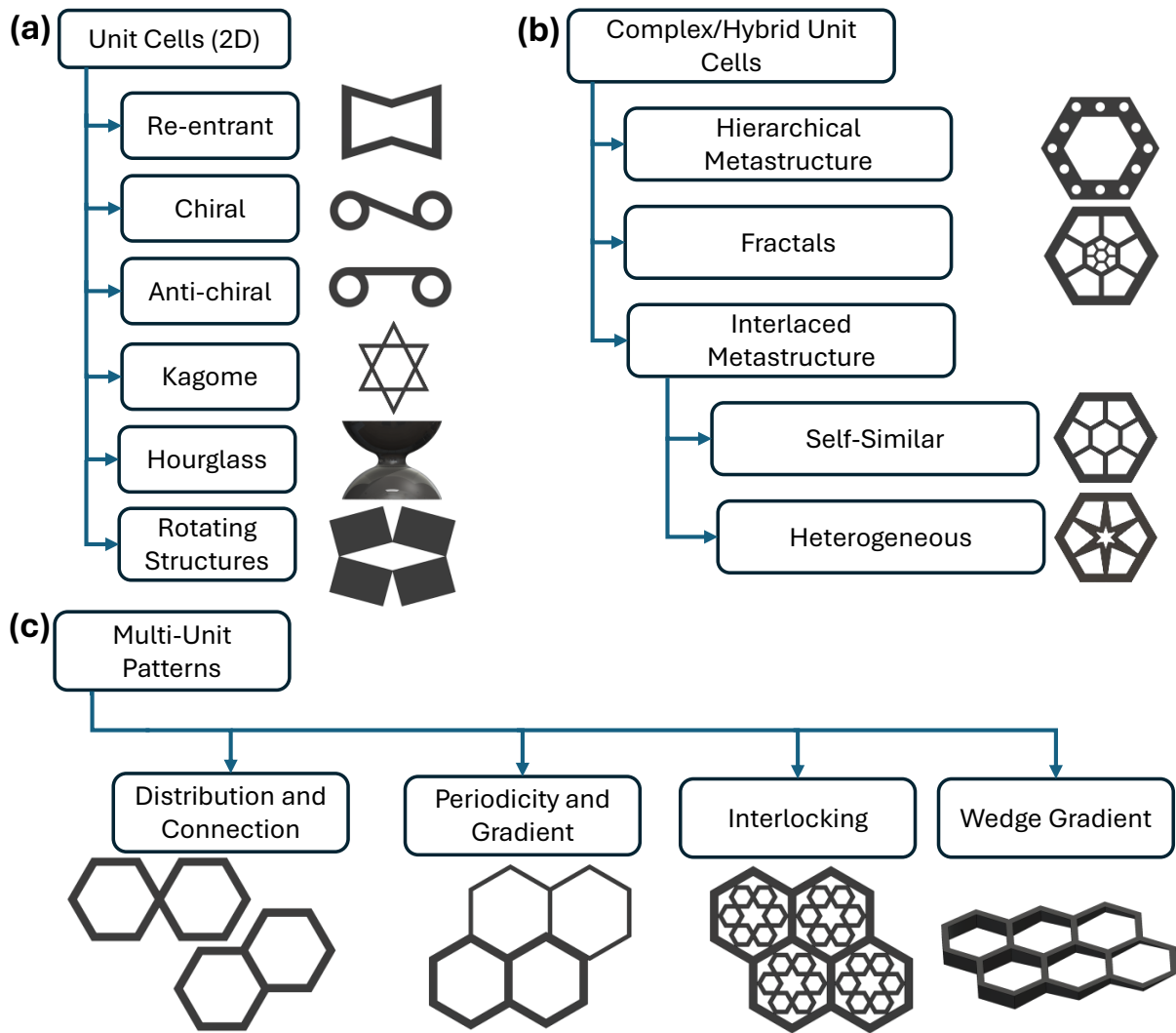


Figure 2: Different types of metastructure unit cells can be categorized based on their lattice structures. (a) Five popular unit cells are used as primary lattices. (b) A complex array of primary lattices can be used to create different possible interesting metastructure unit cells. (c) Multi-unit patterns represent the arrangement of unit cells to form complete 2D and 3D metastructures.

Mechanical properties of simple metastructures such as honeycombs with positive and negative re-entrant angles have been extensively studied through experimental avenues, numerical simulations, and mathematical analyses [39–44]. In recent years, there has been a growing interest in developing engineered materials using a range of 3D and 4D additive manufacturing techniques [45, 46]. Recent advancements in precise additive manufacturing techniques at the microscale have further enabled the fabrication of new lattices with complex topology and interlaced geometry, which are challenging to achieve using traditional subtractive manufacturing methods. Such metastructures have distinct behaviors when subjected to external stimulus such as mechanical excitation [47–53].

Geometric design and pattern have played a significant role in the spiritual traditions of most of the religions. For instance, concentric circles and triangles are widely used as sacred patterns in the Hindu and Buddhist ‘Mandala’; while rectangles and squares are preferred in the ‘Feng Shui’ design of Chinese spiritual tradition. The construction of medieval European cathedrals was often based on the ‘Latin Cross’. Fractal geometries were the most popular design used in the construction of various Hindu temples. The pinnacle of embedding geometric motifs is found in ‘Islamic Geometric Patterns’ which involve more complicated shapes such as hexagons, octagons, decagons, and multi-point stars [54]. One of the interesting applications of such motifs in tessellated form is called ‘Mashrabiya’ which is known to be originated in Baghdad during the 12th-century Abbasid period. Its interlaced arrangements, which

emerged from simplicity and unity of natural as well as geometric motifs, exhibit some fundamental relationships that become in-turn hierarchical or fractal in complex architectures. The architectural applications of ‘Mashrabiya’ had rapidly developed in the medieval Persian and Indian civilizations due to the influence of Islamic religion and mysticism. Such patterns, popularly known as ‘Jali’ in India, were crafted not only for aesthetic purposes but also for their utility in terms of transmitting indirect sunlight, capturing fresh air, passive cooling, maintaining communication with privacy, etc. (some of the patterns are shown in Fig. 1(b-f)). The first instance of developing such patterns in India was found in the Alai Darwaza in the Kutb Minar complex of Old Delhi. The tomb of Itimaduddaula, a magnificent testament to the Mughal style enriches Agra’s vibrant tapestry. Considered as the inspiration for the Taj Mahal, the tomb also known as the ‘Baby Taj Mahal’, is a stunning example of Mughal architecture (Fig. 1 (a)). This mausoleum displays a wonderful variety of geometric arabesques. The strong influence of the Persian style coupled with numerous Indian motifs is visible in this structure. The related lattice structures can be classified based on different unit cell types, considering angle, arrangement, and symmetry (Figure 2(a)). We investigate various interlacing arrangements of these unit cells (Figure 2(b)) and demonstrate how different arrangements can be used to generate complete metastructures (Figure 2(c)). These metastructures provide a foundation for further studies evaluating their performance in controlling elastic wave propagation and vibration. Further, we have developed an AI-based forward analysis model to predict the transmissibility of a metastructure. Also, an AI-based inverse design of metastructure is developed to design new lattices for the desired bandgap creating end-less possibilities of generating suitable patterns focused to an application [55–60].

Results

Dynamic characterization and determination of the Bandgap

Selected latticed metastructures (represented in Fig. 3), generated based on architectural elements (described in Fig. 2) have an overall size of 204 mm x 58 mm and a thickness of 5 mm. The size was carefully chosen keeping in mind the manufacturing constraints as well as the requirement of minimum number of periodic units (greater than 7 units) in the tessellated structure to express the metamaterial behavior [13]. On both sides, 15 mm solid frames are appended with the latticed structure in the longitudinal direction (see Supplementary Fig. S1) for ease of clamping and excitation during dynamic testing. For each latticed structure, there is a frequency band in which the structure may work as an attenuator signifying the absence of wave propagation, and the same is highlighted in Fig. 3. In the middle column (Fig. 3), we have shown the related mode shapes obtained using Ansys corresponding to minimum force transmissibility within the attenuation zone. Different structures have different damping ratios depending on the lattice geometry. The damping ratio is calculated by the half-power bandwidth method (highest for LS1 and the lowest for LS9), which is shown in the supplementary Fig. S11.

Latticed metastructures with different sub-lattice structures are shown in Fig. 4. Figure 4(a-c) illustrates the primary unit cells as honeycomb sub-lattice, single honeycomb, circular pattern of honeycomb cells and star structure respectively. In Figure 4(d), the primary unit cell has a chiral structure with sub-lattices exhibiting a spider web-like pattern. Furthermore, Fig. 4(e) features a primary unit cell as a ring structure interlaced with other ring structures. Figure 4(f) is a fishtail structure. Fig. 4(g) shows the primary unit cell as a series of honeycombs arranged to form a star at the center of the structure. Figure 4(h, i) are combinations of honeycomb and auxetic structure. In the former, these structures are present in a series combination, while in the latter, the auxetic structure is interlaced with the honeycomb structure. The dimensions of the unit cells are detailed in Supplementary Table S1. After creating all the metastructures of specified dimensions, we scaled them up by 1.5 and 2 respectively to capture the scale effect of unit cells in the wave transmission pattern. The scaling effect is illustrated with the help of the Band Gap (BG) ratio in the bar diagram (Fig. 4).

Performance measurement of lattice with resonators

In figure 5, we have selected a primary honeycomb lattice structure interlaced with a single honeycomb unit (LS1) at the centre. Our objective is to study the effect of mass insertion in the central honeycombs on the bandgap characteristics of the metastructure. The metastructure is chosen as per the ease of mass insertion and enables us to observe changes in the attenuation band, which are influenced by local resonances occurring at frequencies that vary with the insertion location. Metallic hexagonal inserts are made up of structural steel (as shown in Supplementary Fig. S5), and their detailed properties and

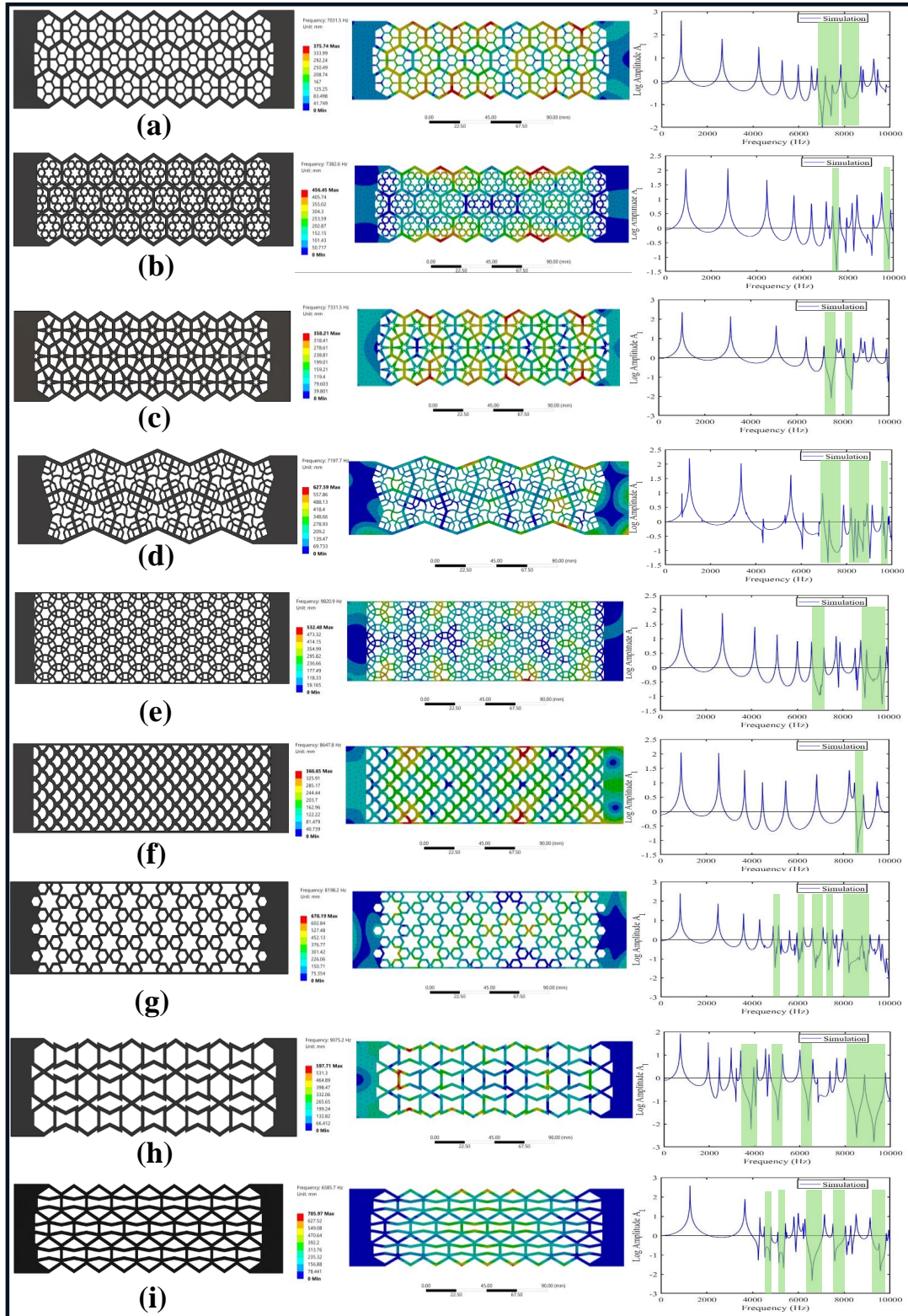


Figure 3: Schematic diagram illustrates latticed mechanical metastructures featuring different interlaced lattice structures (LS1-LS9). Dynamic analysis of the metastructures is performed and mode shapes of lattices at a frequency corresponding to minimum force transmissibility for in-plane excitation are shown. The attenuations corresponding to each geometry are obtained by using the transmissibility plot for each structure. We have highlighted distinct attenuation zones within the transmissibility response of metastructures through green-shaded patches.

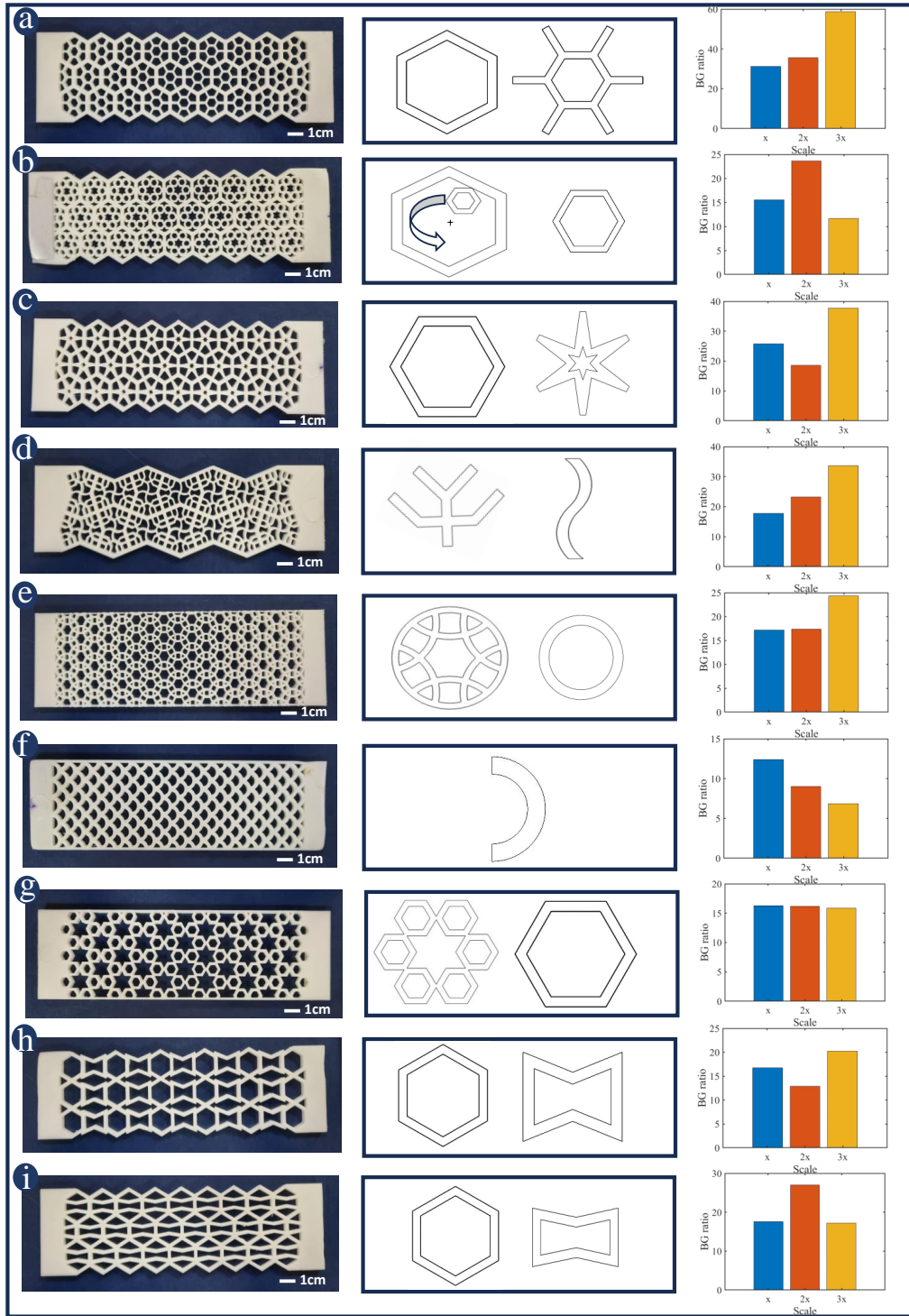


Figure 4: Conducting a comparative analysis, this study investigates the impact of scaling (x, 1.5x, 2x) of the unit cell on the bandgap, with the resulting BG ratio illustrated in a bar diagram. The basic building blocks of unit and sub-unit cells are represented in the middle column of the figure. Subunit cells are used as an interlaced component for the primary structure from which each configuration is constructed. The patterns of latticed mechanical metastructures are 3D Printed using PLA having different primary lattice structures namely (a) Honeycomb-honeycomb interlaced (LS1) (b) Honeycomb interlaced with honeycomb pattern (LS2) (c) Honeycomb interlaced with a star (LS3) (d) Chiral interlaced structure (LS4) (e) Ring interlaced structure (LS5) (f) Fishtail structure (LS6) (g) Star-honeycomb structure (LS7) (h) Honeycomb-auxetic structure (LS8) (i) Honeycomb-auxetic interlaced structure (LS9).

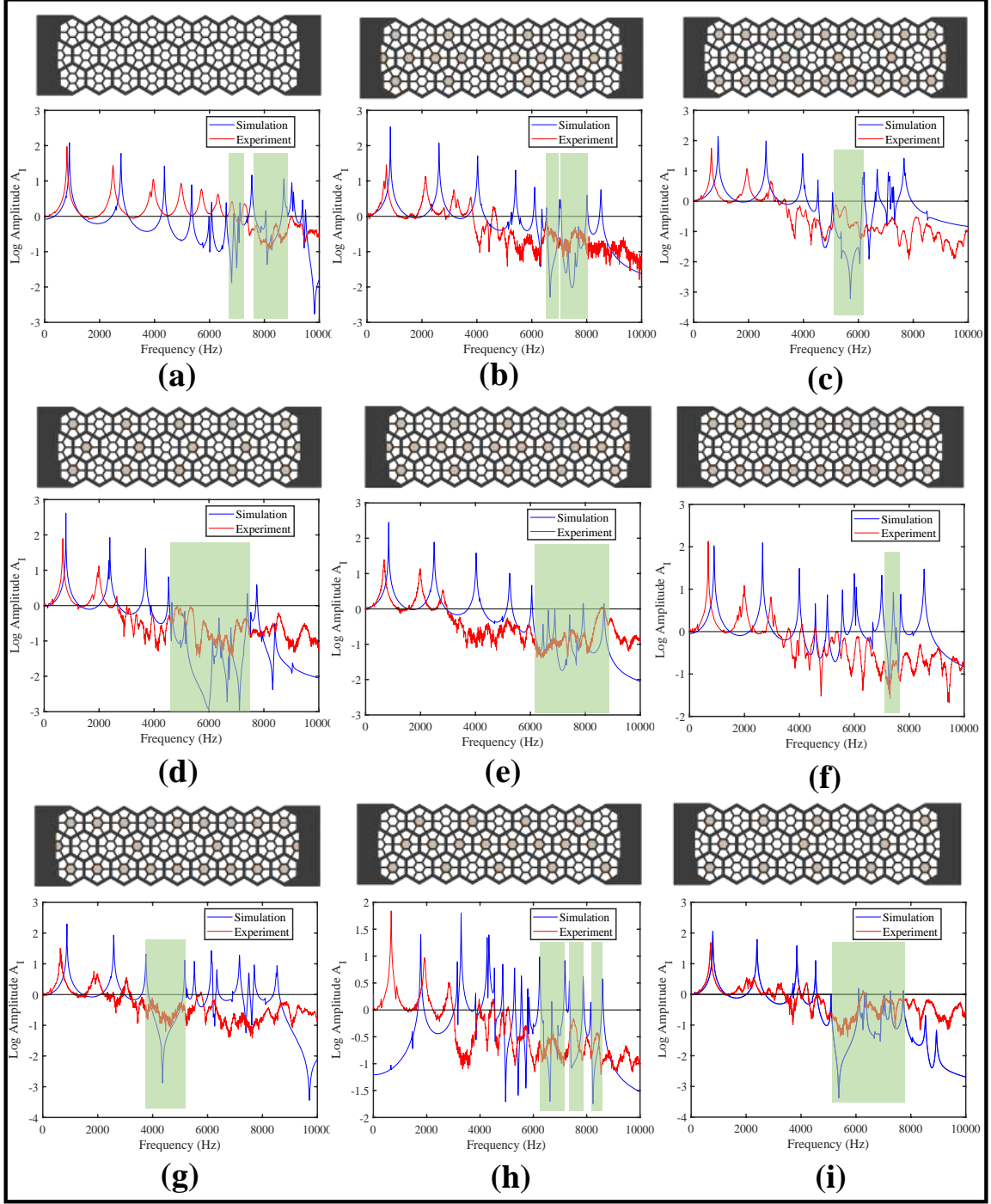


Figure 5: Experimental validation of computational result with variations in mass inserts pattern is shown, and the corresponding bandgaps are marked by green patches. **(a)** Simple interlaced honeycomb structure (LS1) **(b)** Diamond pattern with a broken symmetry at the middle **(c)** Cross pattern **(d)** Forward arrow pattern **(e)** Diamond pattern **(f)** Top and bottom row are filled middle row is empty **(g)** Top and bottom rows are filled with mass inserts while the middle row has two-gap arrangement with no inserts **(h)** Upward pointing arrow pattern **(i)** Top and bottom row inserts are arranged alternatively while middle row has two-gap arrangement with no inserts.

composition are shown in Supplementary table S3. Given that the lattices are fabricated through 3D printing using Polylactic Acid (PLA), and subsequently metallic inserts of much heavier density are used inside the lattice, these inserts function as local resonators due to the density difference between PLA and steel. These characteristics make the metastructure well-suited for vibration control applications. The presence of inserts significantly influences the wave transmission patterns. Furthermore, the strategic placement of the inserts are considered in such a manner that the inserts themselves make a pattern inside the lattice structure. By changing their location, we can control the bandgap for planar excitation in 1D. In Figure 5(a), we present the effect of random vibration through the simple lattice, while in Fig. 5(b) we explore the effect of wave transmission in broken symmetry of diamond pattern where the middle row of the lattice is fully filled while the top and bottom row is filled with metallic inserts with a definite pattern. In Fig. 5(c), the effect of wave transmission in the cross-shape pattern is shown where the inserts are arranged alternatively in the middle row of lattice and the top and bottom row is completely filled. In Fig. 5(d) lattices are filled in such a manner that it forms an arrow indicating towards the right direction. Figure 5(e), represents the diamond pattern where the middle row is fully filled; however, the top and bottom rows are alternatively filled. In Fig. 5(f), the top and bottom rows are fully filled and the middle row is fully empty. In Fig. 5(g), the top and bottom rows are fully filled; however, the middle row is filled such that there is a spacing of two units between the consecutive inserts. In Fig. 5(h), the top row is alternatively filled starting with a blank cell while the bottom row is also alternatively filled starting with a filled cell, and the middle row is fully filled except for the first and the last cell representing upward pointing arrow. In Fig. 5(i), the top and bottom rows are alternatively filled while the middle row is filled with two-unit spacing. Through the study of dynamic response corresponding to harmonic excitation for all these combinations, we aim to find out which pattern location is more sensitive and affects more at a specific frequency range of wave transmission. We observed that generally, the middle row exhibits higher sensitivity compared to the top and bottom rows. Additionally, by arranging different combinations of inserts, we achieved up to 48 % bandgap enlargement, multiple bandgaps, and the ability to shift the bandgap across the desired frequency range. Further, the experiments corresponding to each iteration are carried out to validate our simulation results by using a Laser Doppler Vibrometer (LDV). Random vibration up to 10 KHz is performed using LDS shaker with the gain set as unity. Detailed experimental setup can be seen in Supplementary Fig. S10. As may be observed in Fig. 5, our experimental results show good agreement with the simulation. The printing pattern, and infill density (presented in Supplementary Table S2), also affect the attenuation band.

Bandgap characteristics of honeycomb based interlaced structures

Comparative analysis of the effect of different interlaced structures on bandgap shift (Fig. 6(a)) is carried out in various frequency ranges. The band gap occurs at a frequency band comparatively higher than that of the simple honeycomb structure. Notably, for the LS3 structure bifurcation in bandgap occurs, and for the last structure (LS9) multiple bandgaps occur both for the higher and lower frequency ranges. Furthermore, we have compared the bandgap range of various interlaced honeycomb unit cells (Fig. 6b) along with the force-deflection relationships. The force-deflection relationships are linear for all the patterns except for LS9.

Figure 6(c) illustrates the fractal structure of different order ($n=0,1,2$) and their corresponding bandgap shifts. In different structures, as the fractal order increases, the bandgap shifts to higher frequency ranges, and for further increase in fractal order multiple bandgaps occur. Furthermore, on the right side we have represented the force-deflection relationship for the fractal structure (see Fig. 6d). With the increase in the fractal order, the structure becomes stiffer, with 196.32% increase from zeroth to first-order fractal and 33.61% increase from first to second-order fractal. From this study, we can conclude that with increasing the structural complexity inside the structure, the bandgap starts to shift towards the higher frequency range, and for higher-order fractals, it also bifurcates which is verified by taking different fractal structures inside the honeycomb and explained in the Supplementary Fig. S8.

AI-driven Inverse Design of Metastructures

With the phenomenal expansion potential of the geometry of metastructures, it is possible to use AI efficiently for both forward analysis in predicting the bandgaps as well as inverse design where for a given bandgap a suitable pattern may be obtained. The complete flow diagram of a possible AI-based inverse design of metastructures is depicted in Fig. 7. The entire method comprises two components: (i) the

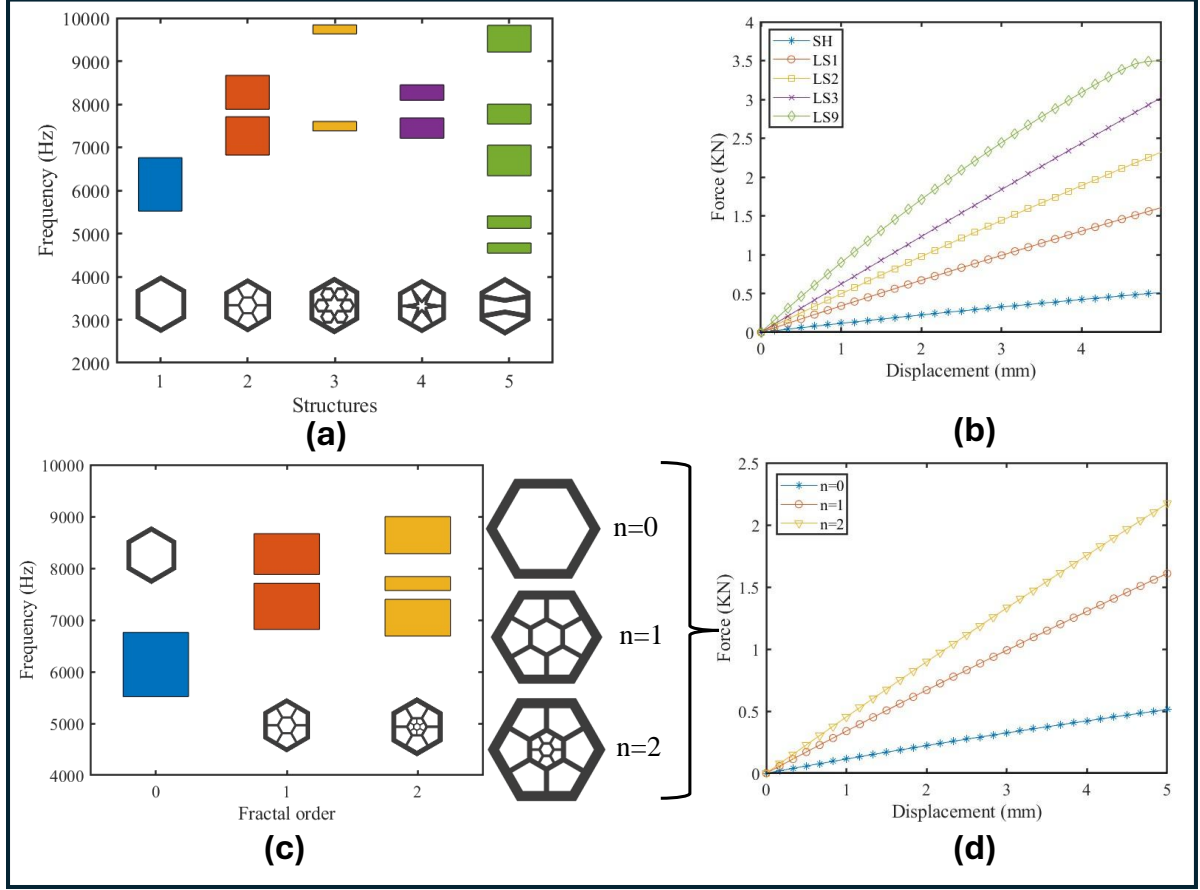


Figure 6: (a) A comparison of bandgap at different frequency levels of different structures interlaced in the honeycomb structure. (b), (d) The comparison of static performance is obtained through analytical computations of different structures. The displacement control mechanism is set as 5 mm compression of initial height of samples (c) Comparison of bandgap in different order ($n=0,1,2$) of the fractal structure.

forward analysis model and (ii) the inverse design model. The forward analysis model acts as a surrogate model for training the inverse design model. It is trained independently for the forward analysis of the metastructures with known transmissibility.

Forward Analysis Model

The forward analysis model consists of repeated blocks of geometric feature extraction modules capable of learning complex metastructure geometry having primary, secondary, and tertiary complexity. Each geometrical feature extraction module consists of a multi-scale geometric attention mechanism having multiple heads of FEM-inspired spatial attention (FSA) blocks. The FSA is designed to learn the dependencies of adjacent connections at different scales using different kernel sizes of convolutional modules. Each FSA consists of an input convolutional layer for feature transformation followed by a spatial attention block [61, 62]. The complete block diagram of the forward analysis block, multi-scale GA module, and the FSA block are provided in the supplementary Figures S13 and S14. The forward analysis model was implemented with 12 layers of geometric feature extraction blocks and 8 heads of FSA in each block. The kernel sizes of the input convolutional layer in 8 FSA heads are selected as (1, 1, 1, 3, 3, 3, 5, 5). This combination of kernel sizes puts more attention on the smallest structures (tertiary), than the secondary, and the primary structures. The output of the geometric features extraction module is processed by a regression head that transforms the geometric features to the transmissibility of dimension (1000, 1). The detailed block diagram and the descriptions are provided in the supplementary file: Fig. S15 and Section E.1.

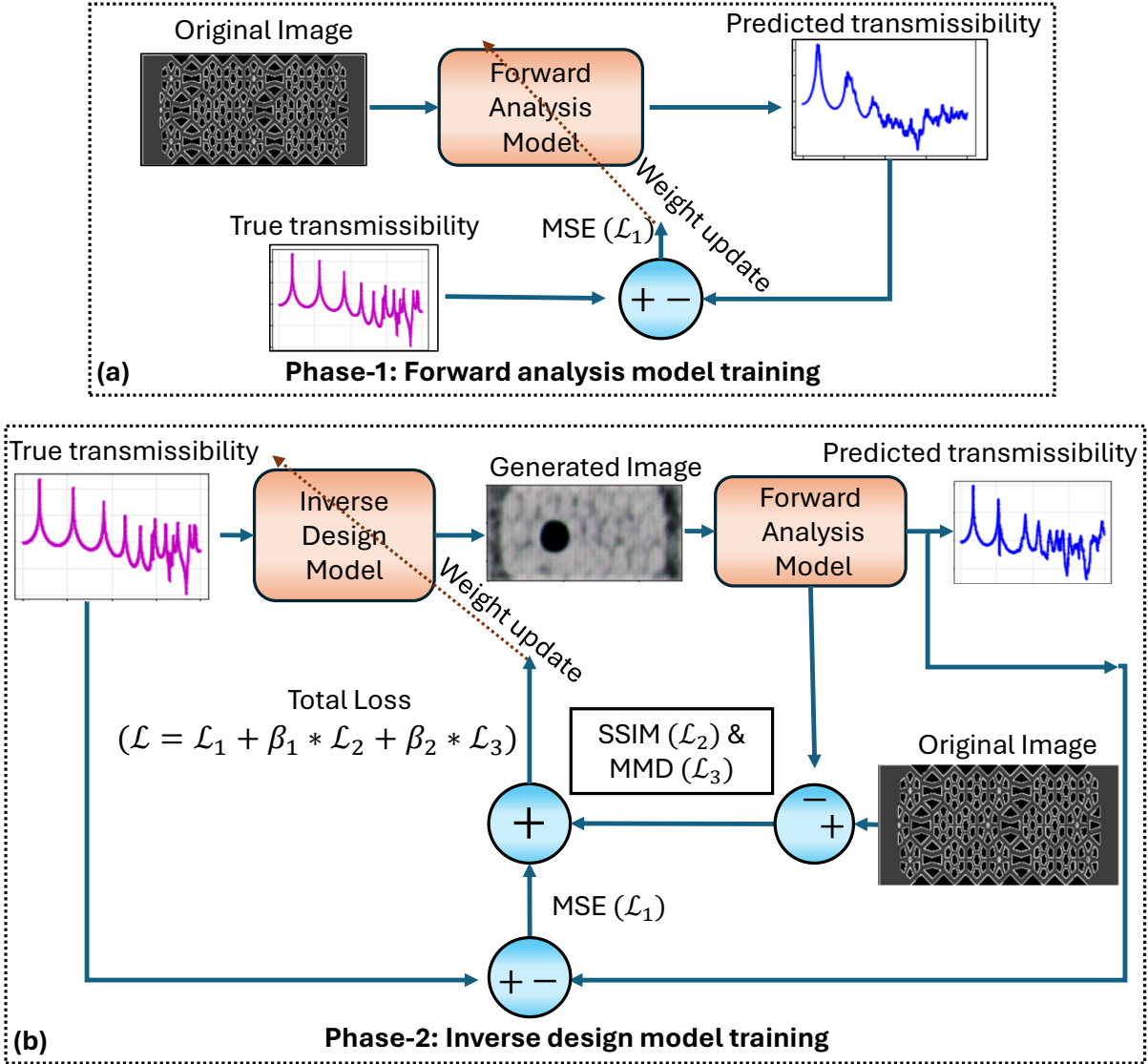


Figure 7: AI-based inverse design of metastructures: (a) Training strategy of forward analysis model to predict the transmissibility for a given metastructure (b) Training strategy of inverse design model to predict the metastructure for given transmissibility spectrum.

Inverse Design Model

The inverse design model is developed to obtain the metastructure geometry using transmissibility plots for the desired bandgap. The detailed block diagram of the inverse design model is provided with the supplementary materials (Figures S16 and S17). The key contributions of the inverse design model are the conversion of transmissibility into latent space using a multi-head 1-D self-attention mechanism, followed by constructing the interlaced patterns using a multiscale residual network. The 1-D self-attention mechanism captures the sequential dependencies of the transmissibility spectrum, [63] and generates a rectified latent space of shape $(3 \times 128 \times 256)$. The latent space is further extended to a new higher space using reflection padding and then non-linearly down-sampled back to the same dimension using multiple consecutive convolutional layers with ReLU activation.

Now the transformed latent space is passed through a multiscale residual network having three parallel convolutional paths with three different kernel sizes: (1×1) , (3×3) , and (5×5) as shown in Fig. S17(b). These sizes have been selected based on the institution to transform the latent space into the three levels of interlaced structural geometry. The smallest kernel is responsible for learning the tertiary structures, the medium size helps to learn the secondary structural geometry. Similarly, the largest value (5×5) is responsible for learning the primary geometry. The final output of the multi-scale residual network is the interlaced patterns. It is now upsampled using three layers of 2-D transposed convolution and then

transformed non-linearly using 2-D convolution and tanh activation to produce the final geometry.

Training

For the training of the proposed AI-based inverse design of the metastructures, a dataset having 720 samples of different metastructures is prepared using different interlaced structures as shown in supplementary Fig. S12. In the unit cell of these structures, the primary structure is a honeycomb and the secondary structures are different combinations of honeycomb, star, circle, hierarchical honeycomb, and auxetic interlaced structure. Then the corresponding transmissibility is calculated using FEM analysis.

The samples are divided into two portions: training and validation with a ratio of 90:10. The AI-based inverse design mechanism is trained in two phases.

- i) **Forward Analysis Model:** In the first phase, the forward analysis model is trained using the training samples to predict the transmissibility of a given metastructures. The training loop is depicted in Fig. 7(a). The comparison of the predicted transmissibility obtained by the forward analysis model and the true transmissibility obtained by the FEM analysis are compared in Fig. 8.
- ii) **Inverse Design Model:** Once the forward analysis model is fully trained, it is used as a surrogate model for the training of the inverse design model as displayed in Fig. 7(b). The loss function (\mathcal{L}) for the weight update of the inverse design model is constructed as provided in equation (1)

$$\mathcal{L} = \mathcal{L}_1 + \beta_1 * \mathcal{L}_2 + \beta_2 * \mathcal{L}_3 \quad (1)$$

where, β_1 and β_2 are the penalty terms for the inclusion of losses \mathcal{L}_2 and \mathcal{L}_3 . The values of β_1 and β_2 were selected as 0.1 and 0.6, respectively.

$\mathcal{L}_1 =$ MSE: mean square error between predicted transmissibility on generated metastructure and the transmissibility obtained from the FEM method on original metastructure.

$\mathcal{L}_2 = 1 -$ SSIM: structural similarity index measure between the generated metastructure and the original metastructure [64].

$\mathcal{L}_3 =$ MMD: maximum mean discrepancy between the generated metastructure and the original metastructure (MMD) [65].

Further details of these losses are provided in the supplementary material, Section F.

Validation of AI-model for metastructure design

The metastructure produced by the inverse design model contains colored noises due to training with a small value of batch size (small batch size was chosen due to the limited number of samples in the dataset). Therefore, a noise removal filter is applied to produce a clear image of the obtained metastructure during validation. The algorithm for the noise removal is provided in supplementary material, Section G. The AI-based inverse design of metastructures is validated under two cases:

Validation on known metastructure as test sample:

The comparison of generated metastructure for one test sample from the test data (10% of available 720 samples) is provided in Fig. 8. Figures 8(a), (b) show the test metastructure and its transmissibility obtained by the FEM method which is assumed to be true (input) transmissibility for inverse design. The predicted metastructure by the inverse design model exactly matches the original metastructure with an SSIM score of 0.991 as shown in Figure 8(c). Forward analysis is performed on both the original and the predicted metastructures. The predicted transmissibilities are compared with the input (true) transmissibility in Fig. 8(d) and (e). It can be observed that MSEs for transmissibility obtained from the original metastructure and the predicted metastructure are 0.0834 and 0.1939 respectively. The MSE for predicted transmissibility by forward analysis on the predicted metastructure is comparatively larger because of the existence of noises in the predicted metastructure.

Validation on Artificial Transmissibility:

The AI-based inverse design model is further validated for practical deployment to design a metastructure facilitating the formation of a desired frequency bandgap. Hence, an artificial transmissibility is created having the desired bandgap and fed to the inverse design model. The generated metastructure and the corresponding transmissibilities obtained by the forward analysis model and FEM are shown in

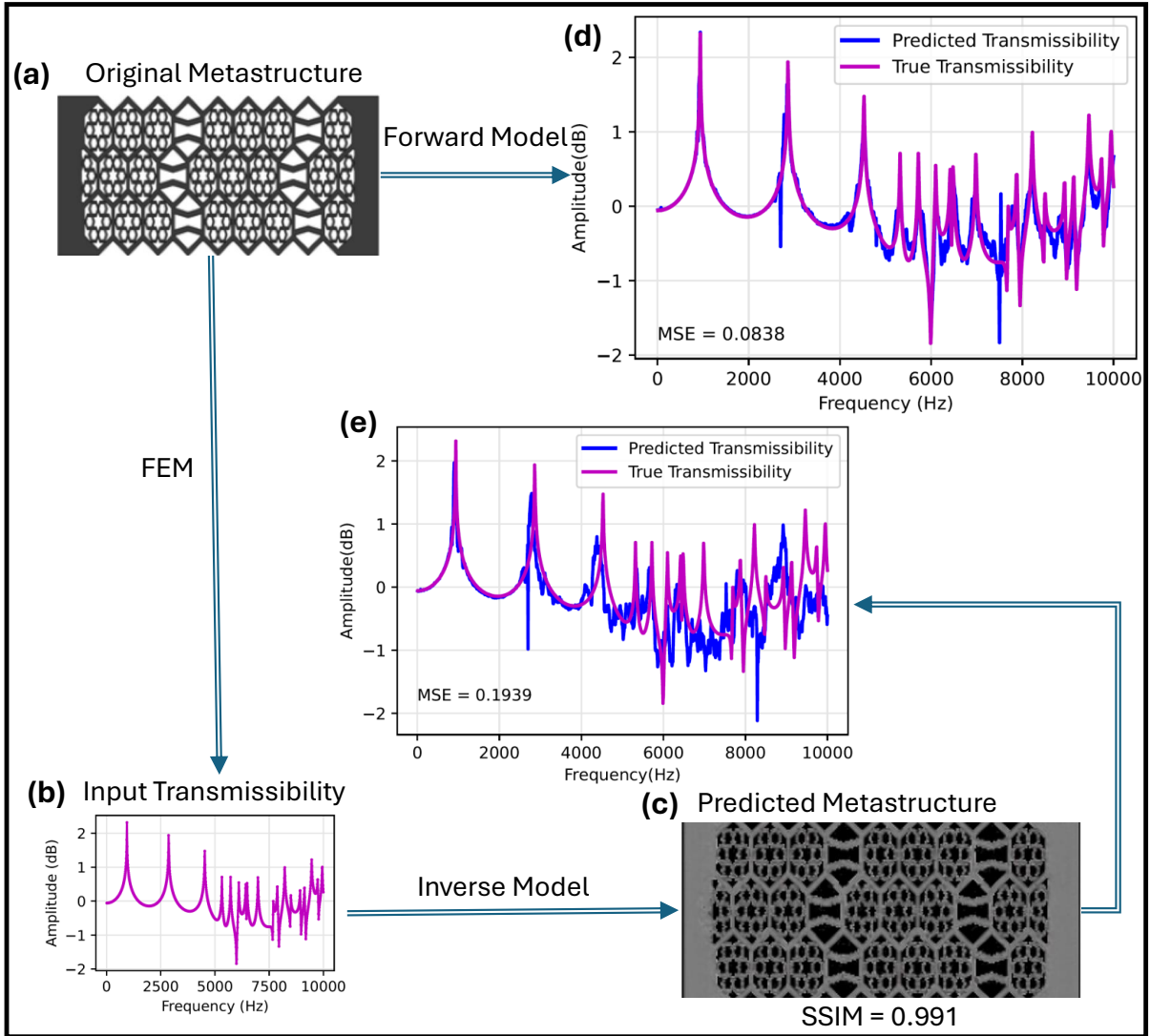


Figure 8: **Validation results for AI-based inverse design of metastructure.** (a) Original metastructure of the test sample. (b) Input transmissibility obtained by FEM for the original metastructure. (c) Metastructure predicted (generated) by the inverse design model using the input transmissibility. SSIM = 0.991, closer to unity validates the exact match with the original image. (d) Comparing the transmissibilities of the original metastructure obtained from the forward model and FEM. (e) Comparing the transmissibilities of the generated metastructure obtained from the forward model and FEM.

Fig. 9. The obtained metastructure is the combination of a honeycomb and hierarchical honeycomb substructures. The MSE between the predicted transmissibility and the input transmissibility is 0.7408.

Discussion

It has been found experimentally and analytically from the previous study that a simple lattice structure has the ability to block waves for a certain frequency range when it passes longitudinally throughout the lattice. Inspired from the architectural patterns, we have designed mechanical metamaterial lattices with diverse interlaced structures. A comprehensive study has been performed through simulation-based analysis using Ansys. Experiments have been conducted to validate the transmissibility property corresponding to different lattice configurations. This work shows the blueprint of metamaterials, including the fact that the effective properties of the lattice are contingent on collective patterns and subpatterns of the unit cells. Furthermore, the tunability of the bandgaps through design resulted in larger and multiple bandgaps occurring in Frequency Response Function (FRF) plots. The reported band gap caused by the lattice structures can be further modified by adding metallic inserts with different combinations

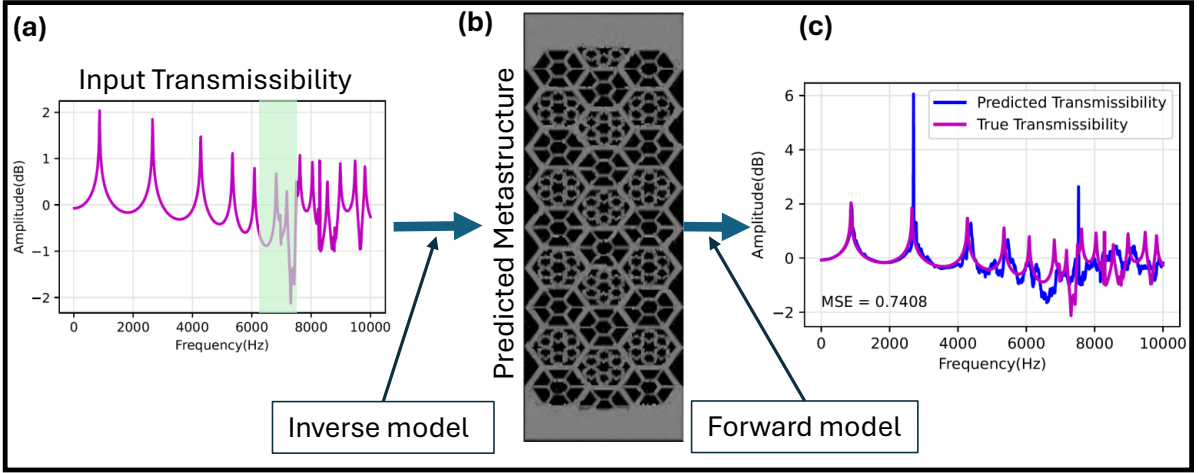


Figure 9: **AI-based inverse design of metastructure for a desired bandgap.** (a) Artificial (input) transmissibility having the desired bandgap as highlighted. (b) The generated metastructure obtained from the inverse design model, which facilitates the desired bandgap. (c) Validation of the generated metastructure design by comparing the transmissibilities obtained by the forward analysis model and by the FEM.

of insert patterns. These metallic inserts interact with the geometry and due to the large density difference as compared to lattice material (PLA), they act as local resonators, providing flexibility to adjust bandgaps. Some significant negative peaks are obtained from the transmissibility plots that signify wave attenuation and show good agreement with the simulation results, as shown in Fig. 5. The discrepancy in some amplitude and peak are due to nonconsideration of damping in simulation. Apart from damping, printing speed, orientation, infill pattern, and infill density of 3D printing are also affected as discussed and shown in Supplementary Table S2. These findings unveil a deep connection between lattices and band gaps and have broad potential applications in the field of vibration isolation for high-speed trains and in serving as surface waveguides and absorbers.

The second part of this study on the inverse design of metastructure using geometric attention-based deep architecture is a benchmark in the field of inverse design of complex structure whether it is metastructure for the desired mechanical response or any other complex pattern for desired physical properties. The major challenge in the training of an AI-based inverse design model is the availability of sufficient number of training samples. The higher the complexity of the structure, the higher the number of samples required for the training. Our proposed model uses FEM to learn the dependencies of adjacent connections in the geometrical structure. Therefore, it can easily extract the information embedded in the complex structure and learn the relationship between the input geometry and the output transmissibility. Further, the multiscale geometrical attention mechanism provides the capability to learn the multiple levels of complexity. With the same concept, multiscale feature transformation using the multiscale residual network enables the inverse design model to reconstruct multiple levels of geometry, like a honeycomb and hierarchical honeycomb substructures. Therefore, the proposed framework of the geometrical attention-based feature learning and the inverse design can be useful for any other scientific design problem.

In summary, our paper reflects the following novelties:

- Discovery of novel functionality in a set of ancient patterns from the mechanical metastructure perspective such as vibration transmission and attenuation.
- Identification of two unique parameters: interlaced metastructure and fractal order in such patterns followed by their application in 3D printed 2D mechanical metastructure panels.
- Further modifications of such metastructures by including local resonators in the form of mass inserts to improve bandgap characteristics through experimental studies.
- Creation of novel AI-based forward analysis model using multiscale geometric attention mechanism which can predict the transmissibility as well as bandgap of a metastructure subjected to base excitation.

- The newly developed model is highly efficient as it is trained only on 648 sample patterns (90 % of 720 numerically generated dataset). This results in predicting the transmissibility with mean square error of 0.08 while in similar literatures, ML models were generally trained on 5000 to 40000 data sets to achieve similar level of accuracy.
- Further, we have been able to create complex multiscale patterns successfully and predict their bandgap characteristics through the transmissibility plot using the current AI model. We believe this will facilitate the generation of many customizable complex patterns for mechanical metastructures efficiently.
- A novel inverse design model of metastructure based on NLP inspired multiheaded attention mechanism with 1D position encoding and multiscale residual network has also been demonstrated by providing artificial transmissibility for a desired frequency bandgap. The inverse design model is found to be much more efficient to reconstruct the complex metastructure with similarity index of 0.991.

Conclusions

This research study highlights the translational application potential of vast range of patterns and motifs developed in the field of architecture into the metamaterial-based wave attenuation. Thus, the utilitarian values of aesthetic constructs in the field of vibration and sound engineering may open up new systems for wave control including bandwidth control, subwavelength acoustic imaging, and generation of acoustic black holes. Additionally, a systematic investigation process has been created on the basis of root lattice identification, multi-scale lattice formation through a hierarchic system, development of hybrid lattice structure, and the effect of interlacing in the vibration mitigation potential initiated from the historic geometric patterns found in the tomb of I'timad-ud-Daulla. In general, the simple lattice structures typically act as attenuators, however, this study demonstrates that the interlaced structure offers an enhanced vibration attenuation property depending on the interlace geometry with improved control over the attenuation frequency range. Such effects can be further enhanced, in the presence of and through strategic positioning of the metallic inserts inside the lattice structure which may result in significant expansion of the bandwidth. This method has been enhanced with the help of AI-based inverse design models to predict metastructures that exhibit the desired bandgap and the corresponding transmissibility. Although this study concentrates on predominantly honeycomb-shaped interlaced structures, the principle of incorporating mass resonators can be applied to other geometries to manipulate bandgap frequencies. Moreover, the concept may be extended to three-dimensional interlaced structures with diverse lattice and interlace configurations across multiple length scales. Another possibility of future expansion is related to the insertion of smart materials in the lattice structure such that the stiffness and the damping can be controlled over time; thus, transforming it into 4-D metamaterial.

Methods

Experimental testing

The study utilizes a non-contact technique to measure vibration to assess the response of different latticed metastructures. Nine 3D printed samples, each showing unique metastructure, are subjected to dynamic testing using a 3D Laser Doppler vibrometer (LDV) from Polytec (Details of the experimental setup presented in Supplementary Fig. S10). These samples are attached to an Electrodynamic shaker system in cantilever mode. The laser head of LDV captures surface velocity by analyzing the phase shift between the incident and reflected laser beams. Data acquisition and signal processing are executed through the NI-DAQ system. The base excitation technique is utilized to determine transmissibility. In this method, the LDS shaker generates 3200 Fast Fourier Transform (FFT) lines, and the pseudo-random excitation with a frequency range of 0 to 10 KHz. Displacements of the top and bottom surfaces of the samples are recorded to calculate transmissibility after post-processing of the data.

Finite element simulations

Finite element analysis-based simulation has been carried out using Ansys, employing the Ansys Parametric Design Language (APDL) solver for all the nine structures, and the host material is chosen as

PLA (detailed properties given in Supplementary Table S3). The entire structure was discretized by using tetrahedron elements with a 2 mm element size, to ensure convergence for interlaced geometries. The smaller edges of the base structure were fixed, while the longer edges remained free. A dynamic force of amplitude 10 N was applied to the base, and the response was calculated on the opposite phase. Modal analysis was performed to identify all modes up to 10 KHz frequency, followed by harmonic analysis to obtain the transmissibility. The mode superposition method was used to link the modal analysis results with the harmonic analysis input. Frequency response functions (FRFs) were generated over the frequency range of 0 to 10 KHz with a 10 Hz frequency resolution; this step size is preferable to accurately capture the response. A structural damping ratio of 0.001 was incorporated to account for the viscoelastic effect of PLA substrate.

Data and code availability

All relevant data and codes will be available upon reasonable request from the contact author. The research data are presented either in the main file or in a supplementary file.

References

- [1] U. Leonhardt, “Invisibility cup,” *Nature photonics*, vol. 1, no. 4, pp. 207–208, 2007.
- [2] C. S. Ha, D. Yao, Z. Xu, C. Liu, H. Liu, D. Elkins, M. Kile, V. Deshpande, Z. Kong, M. Bauchy, *et al.*, “Rapid inverse design of metamaterials based on prescribed mechanical behavior through machine learning,” *Nature Communications*, vol. 14, no. 1, p. 5765, 2023.
- [3] G. Ma and P. Sheng, “Acoustic metamaterials: From local resonances to broad horizons,” *Science Advances*, vol. 2, p. e1501595, 02 2016.
- [4] J. L. Silverberg, A. A. Evans, L. McLeod, R. C. Hayward, T. Hull, C. D. Santangelo, and I. Cohen, “Using origami design principles to fold reprogrammable mechanical metamaterials,” *science*, vol. 345, no. 6197, pp. 647–650, 2014.
- [5] A. Dwivedi and S. A. Horsley, “Line waves in elastic metamaterials,” in *ASME International Mechanical Engineering Congress and Exposition*, vol. 87684, p. V011T12A013, American Society of Mechanical Engineers, 2023.
- [6] L. Ai and X.-L. Gao, “Metamaterials with negative poisson’s ratio and non-positive thermal expansion,” *Composite Structures*, vol. 162, pp. 70–84, 2017.
- [7] S. Horsley and A. Dwivedi, “Theory of electromagnetic line waves,” *Physical Review B*, vol. 108, no. 15, p. 155437, 2023.
- [8] V. Nikkhah, A. Pirmoradi, F. Ashtiani, B. Edwards, F. Aflatouni, and N. Engheta, “Inverse-designed low-index-contrast structures on a silicon photonics platform for vector–matrix multiplication,” *Nature Photonics*, pp. 1–8, 2024.
- [9] E. Panahi, A. Hosseinkhani, M. F. Khansanami, D. Younesian, and M. Ranjbar, “Novel cross shape phononic crystals with broadband vibration wave attenuation characteristic: Design, modeling and testing,” *Thin-Walled Structures*, vol. 163, p. 107665, 2021.
- [10] C. Sugino, S. Leadenham, M. Ruzzene, and A. Erturk, “On the mechanism of bandgap formation in locally resonant finite elastic metamaterials,” *Journal of Applied Physics*, vol. 120, no. 13, 2016.
- [11] X. Liu, G. Hu, C. Sun, and G. Huang, “Wave propagation characterization and design of two-dimensional elastic chiral metacomposite,” *Journal of Sound and Vibration*, vol. 330, no. 11, pp. 2536–2553, 2011.
- [12] A. Dwivedi, A. Banerjee, and B. Bhattacharya, “Simultaneous energy harvesting and vibration attenuation in piezo-embedded negative stiffness metamaterial,” *Journal of Intelligent Material Systems and Structures*, vol. 31, no. 8, pp. 1076–1090, 2020.

- [13] A. Dwivedi, A. Banerjee, S. Adhikari, and B. Bhattacharya, “Optimal electromechanical bandgaps in piezo-embedded mechanical metamaterials,” *International Journal of Mechanics and Materials in Design*, vol. 17, no. 2, pp. 419–439, 2021.
- [14] L. Ai and X.-L. Gao, “Metamaterials with negative poisson’s ratio and non-positive thermal expansion,” *Composite Structures*, vol. 162, pp. 70–84, 2017.
- [15] F. Li and R. Hu, “Metamaterials-enabled sensing for human-machine interfacing,” *Sensors*, vol. 21, no. 1, p. 161, 2020.
- [16] D. Yigci, A. Ahmadpour, and S. Tasoglu, “Ai-based metamaterial design for wearables,” *Advanced Sensor Research*, vol. 3, no. 3, p. 2300109, 2024.
- [17] C. Brendel, V. Peano, O. Painter, and F. Marquardt, “Snowflake phononic topological insulator at the nanoscale,” *Physical Review B*, vol. 97, 01 2018.
- [18] W. Chuang, Z. Jihong, W. Manqiao, H. Jie, Z. Han, M. Lu, L. Chenyang, and W. Zhang, “Multi-scale design and optimization for solid-lattice hybrid structures and their application to aerospace vehicle components,” *Chinese Journal of Aeronautics*, vol. 34, no. 5, pp. 386–398, 2021.
- [19] Z. Jia, F. Liu, X. Jiang, and L. Wang, “Engineering lattice metamaterials for extreme property, programmability, and multifunctionality,” *Journal of Applied Physics*, vol. 127, p. 150901, 04 2020.
- [20] X. Chen, Q. Ji, J. A. I. Martinez, H. Tan, G. Ulliac, V. Laude, and M. Kadic, “Closed tubular mechanical metamaterial as lightweight load-bearing structure and energy absorber,” *Journal of the Mechanics and Physics of Solids*, vol. 167, p. 104957, 2022.
- [21] J. Sun, E. Lerner, B. Tighe, C. Middlemist, and J. Zhao, “Embedded shape morphing for morphologically adaptive robots,” *Nature Communications*, vol. 14, no. 1, p. 6023, 2023.
- [22] C. Tawk, R. Mutlu, and G. Alici, “A 3d printed modular soft gripper integrated with metamaterials for conformal grasping,” *Frontiers in Robotics and AI*, vol. 8, p. 799230, 2022.
- [23] C. Lim, J. Reddy, *et al.*, “Built-up structural steel sections as seismic metamaterials for surface wave attenuation with low frequency wide bandgap in layered soil medium,” *Engineering Structures*, vol. 188, pp. 440–451, 2019.
- [24] T. Guner, O. S. Bursi, and M. Broccardo, “Seismic vibration mitigation of steel storage tanks by metafoundations endowed with linear and bistable columns,” *Bulletin of Earthquake Engineering*, vol. 22, no. 1, pp. 29–54, 2024.
- [25] “The cylindrical mechanical metamaterial with high-level thermal-mechanical stabilities and high dynamic stiffness,” *Mechanics of Materials*, vol. 186, p. 104799, 2023.
- [26] X. Hu, “Analytic model of elastic metamaterials with local resonances,” *Phys. Rev. B*, vol. 79, 05 2009.
- [27] A. Dwivedi, A. Banerjee, and B. Bhattacharya, “A novel approach for maximization of attenuation bandwidth of the piezo-embedded negative stiffness metamaterial,” in *Active and passive smart structures and integrated systems XIV*, vol. 11376, pp. 478–485, SPIE, 2020.
- [28] C. Morris, L. Bekker, C. Spadaccini, M. Haberman, and C. Seepersad, “Tunable mechanical metamaterial with constrained negative stiffness for improved quasi-static and dynamic energy dissipation,” *Advanced Engineering Materials*, vol. 21, 04 2019.
- [29] A. Farzaneh, N. Pawar, C. M. Portela, and J. B. Hopkins, “Sequential metamaterials with alternating poisson’s ratios,” *Nature Communications*, vol. 13, 02 2022.
- [30] A. Singh, T. Mukhopadhyay, S. Adhikari, and B. Bhattacharya, “Active multi-physical modulation of poisson’s ratios in composite piezoelectric lattices: on-demand sign reversal,” *Composite Structures*, vol. 280, p. 114857, 2022.
- [31] Q. Zhang and Y. Sun, “Novel metamaterial structures with negative thermal expansion and tunable mechanical properties,” *International Journal of Mechanical Sciences*, vol. 261, p. 108692, 2024.

- [32] Y. Chen, “Broadband one-dimensional photonic crystal wave plate containing single-negative materials,” *Optics express*, vol. 18, pp. 19920–9, 09 2010.
- [33] J. Pendry, “Negative refraction makes a perfect lens,” *Physical review letters*, vol. 85, pp. 3966–9, 11 2000.
- [34] C. Goffaux and J. Vigneron, “Theoretical study of a tunable phononic band gap system,” *Phys. Rev. B*, vol. 64, 07 2001.
- [35] L. D’Alessandro, A. Krushynska, R. Ardito, N. Pugno, and A. Corigliano, “A design strategy to match the band gap of periodic and aperiodic metamaterials,” *Scientific Reports*, 10 2020.
- [36] A. Dwivedi, R. K. Munian, B. Bhattacharya, and S. Adhikari, “Bandgap formation mechanism in tacticity inspired elastic mechanical metastructures,” *Scientific Reports*, vol. 14, no. 1, p. 24611, 2024.
- [37] A. Sarychev and V. Shalaev, *Electrodynamics of Metamaterials*. 01 2007.
- [38] P. Jiao, J. Mueller, J. Raney, X. Zheng, and A. Alavi, “Mechanical metamaterials and beyond,” *Nature Communications*, vol. 14, 09 2023.
- [39] V. Gupta, S. Adhikari, and B. Bhattacharya, “Exploring the dynamics of hourglass shaped lattice metastructures,” *Scientific Reports*, vol. 10, 12 2020.
- [40] L. Yang, O. Harrysson, H. West, and D. Cormier, “Mechanical properties of 3d re-entrant honeycomb auxetic structures realized via additive manufacturing,” *International Journal of Solids and Structures*, vol. 69-70, pp. 475–490, 2015.
- [41] Y. Jiang and Y. Li, “3d printed auxetic mechanical metamaterial with chiral cells and re-entrant cores,” *Scientific Reports*, vol. 8, 02 2018.
- [42] M. Xu, Z. Zhao, P. Wang, S. Duan, H. Lei, and D. Fang, “Mechanical performance of bio-inspired hierarchical honeycomb metamaterials,” *International Journal of Solids and Structures*, vol. 254-255, p. 111866, 2022.
- [43] A. Dwivedi, A. Banerjee, and B. Bhattacharya, “Dynamics of piezo-embedded negative stiffness mechanical metamaterials: A study on electromechanical bandgaps,” in *ASME International Mechanical Engineering Congress and Exposition*, vol. 84478, p. V001T01A015, American Society of Mechanical Engineers, 2020.
- [44] T. Shimada, L. Lich, K. Nagano, J. Wang, and T. Kitamura, “Hierarchical ferroelectric and ferrotoroidic polarizations coexistent in nano-metamaterials,” *Scientific Reports*, vol. 5, p. 14653, 10 2015.
- [45] B. B. Samal, A. Jena, S. K. Varshney, and C. S. Kumar, “4d printing of shape memory polymers: a comparative study of programming methodologies on various material properties,” *Smart Materials and Structures*, vol. 32, no. 7, p. 074003, 2023.
- [46] T. van Manen, S. Janbaz, K. M. Jansen, and A. A. Zadpoor, “4d printing of reconfigurable metamaterials and devices,” *Communications Materials*, vol. 2, no. 1, p. 56, 2021.
- [47] I. Arretche and K. H. Matlack, “On the interrelationship between static and vibration mitigation properties of architected metastructures,” *Frontiers in Materials*, vol. 5, p. 68, 2018.
- [48] A. Dwivedi, A. Banerjee, S. Adhikari, and B. Bhattacharya, “Bandgap merging with double-negative metabeam,” *Mechanics Research Communications*, vol. 122, p. 103889, 2022.
- [49] G. Aguzzi, C. Kanellopoulos, R. Wiltshaw, R. V. Craster, E. N. Chatzi, and A. Colombi, “Octet lattice-based plate for elastic wave control,” *Scientific reports*, vol. 12, no. 1, p. 1088, 2022.
- [50] T. Doehring, W. Nelson, T. Harris, and A. Freed, “Fe vibration analyses of novel conforming metastructures and standard lattices for simple bricks and a topology-optimized aerodynamic bracket,” *Scientific reports*, vol. 10, no. 1, p. 21484, 2020.

- [51] T. Gupta, V. Gupta, and B. Bhattacharya, “Tailoring of interface mode with actively controlled sma spring,” in *Active and Passive Smart Structures and Integrated Systems XVIII*, vol. 12946, pp. 451–457, SPIE, 2024.
- [52] H. Mirani, V. Gupta, S. Adhikari, and B. Bhattacharya, “Tailoring of interface modes in topologically protected edge states with hourglass lattice metamaterials,” *Journal of Sound and Vibration*, vol. 562, p. 117814, 2023.
- [53] C. Sirote-Katz, D. Shohat, C. Merrigan, Y. Lahini, C. Nisoli, and Y. Shokef, “Emergent disorder and mechanical memory in periodic metamaterials,” *Nature Communications*, vol. 15, no. 1, p. 4008, 2024.
- [54] P. R. Cromwell, “Modularity and hierarchy in persian geometric ornament,” *Nexus network journal*, vol. 18, pp. 7–54, 2016.
- [55] R. Pestourie, Y. Mroueh, T. V. Nguyen, P. Das, and S. G. Johnson, “Active learning of deep surrogates for pdes: application to metasurface design,” *npj Computational Materials*, vol. 6, no. 1, p. 164, 2020.
- [56] W. Deng, S. Kumar, A. Vallone, D. M. Kochmann, and J. R. Greer, “Ai-enabled materials design of non-periodic 3d architectures with predictable direction-dependent elastic properties,” *Advanced Materials*, p. 2308149, 2024.
- [57] Y. Wang, Q. Zeng, J. Wang, Y. Li, and D. Fang, “Inverse design of shell-based mechanical metamaterial with customized loading curves based on machine learning and genetic algorithm,” *Computer Methods in Applied Mechanics and Engineering*, vol. 401, p. 115571, 2022.
- [58] X. Zheng, T.-T. Chen, X. Guo, S. Samitsu, and I. Watanabe, “Controllable inverse design of auxetic metamaterials using deep learning,” *Materials & Design*, vol. 211, p. 110178, 2021.
- [59] M. Maurizi, C. Gao, and F. Berto, “Inverse design of truss lattice materials with superior buckling resistance,” *npj Computational Materials*, vol. 8, no. 1, p. 247, 2022.
- [60] A. E. Gongora, C. Friedman, D. K. Newton, T. D. Yee, Z. Doorenbos, B. Giera, E. B. Duoss, T. Y.-J. Han, K. Sullivan, and J. N. Rodriguez, “Accelerating the design of lattice structures using machine learning,” *Scientific Reports*, vol. 14, no. 1, p. 13703, 2024.
- [61] S. Woo, J. Park, J.-Y. Lee, and I. S. Kweon, “Cbam: Convolutional block attention module,” in *Computer Vision – ECCV 2018* (V. Ferrari, M. Hebert, C. Sminchisescu, and Y. Weiss, eds.), (Cham), pp. 3–19, Springer International Publishing, 2018.
- [62] L. Gao, X. Li, D. Liu, L. Wang, and Z. Yu, “A bidirectional deep neural network for accurate silicon color design,” *Advanced Materials*, vol. 31, no. 51, p. 1905467, 2019.
- [63] A. K. Sharma and N. K. Verma, “A novel vision transformer with residual in self-attention for biomedical image classification,” 2023.
- [64] Z. Wang, A. Bovik, H. Sheikh, and E. Simoncelli, “Image quality assessment: from error visibility to structural similarity,” *IEEE Transactions on Image Processing*, vol. 13, no. 4, pp. 600–612, 2004.
- [65] A. K. Sharma and N. K. Verma, “Quick learning mechanism with cross-domain adaptation for intelligent fault diagnosis,” *IEEE Transactions on Artificial Intelligence*, vol. 3, no. 3, pp. 381–390, 2022.

Acknowledgements

The authors want to thank Mr. Gyanendra Prakesh Tripathi, who provided insight to conduct the experiments, and Mr. Abhishek Kumar Singh, who helped to 3D print the samples. The photo credits for Figure 1(a-f) are given to Chitrlekha Bhattacharya and Bipasana Bhattacharya.

Author information

Authors and Affiliations

Department of Mechanical Engineering, Indian Institute of Technology Kanpur, India

Bishakh Bhattacharya, Tanuj Gupta, Arun Kumar Sharma, Ankur Dwivedi, Subhadeep Sahana, Ashish Awasthi

Department of Precision and Microsystems Engineering, Delft University of Technology, Netherland

Vivek Gupta

Department of Mechanical Engineering, Motilal Nehru National Institute of Technology Allahabad, India

Suryansh Pathak

Author contribution

Bishakh Bhattacharya: Conceived the primary idea, reviewed the manuscript, critically examined the results, checked the data, wrote the manuscript, and acquired funding. **Tanuj Gupta:** Expanded the idea jointly, modeled all the structures and designed and performed numerical simulations. Fabricated the samples and carried out related experiments and material testing, documented the results, reviewed the manuscript, critically examined the results, and checked the data, wrote the manuscript. **Arun Kumar Sharma:** Conceived the idea of AI-based inverse design of metastructures, and implemented a new strategy of feature learning using multiscale Geometric Attention and the idea of reproducing the geometry with multiple levels of complexity using the multiscale residual network. Code Implementation, training, and validation of the AI models and writing the AI-based inverse design in the manuscript. Critically examined the manuscript. **Ankur Dwivedi:** Expanded the idea jointly in inverse design, critically examined the results, checked the data, and wrote the manuscript. **Vivek Gupta:** Expanded the idea jointly, reviewed the manuscript, critically examined the results, checked the data, and wrote the manuscript. **Subhadeep Sahana:** Carried out numerical simulations to generate synthetic data for training the AI model and critically analyzed the paper for logical conclusions. **Suryansh Pathak:** Conducted the experiments, performed numerical simulations, and checked the data. **Ashish Awasthi:** Carried out numerical simulations to generate synthetic data for training the AI model.

Competing interest

The authors declare no competing interests.